Journal of
Applied
Crystallography

ISSN 1600-5767

Received 1 July 2014
Accepted 16 February 2015

Enhancement of thermoelectric figure of merit in Bi_2Se_3 crystals through a necking process

Shashikant Gupta,[a,b] N. Vijayan,[b] Anuj Krishna,[b,c] Kanika Thukral,[b,c] K. K. Maurya,[b] Saravanan Muthiah,[d] Ajay Dhar,[d] Budhendra Singh[e] and G. Bhagavannarayana[b]*

[a]Deenbandhu Chhotu Ram University of Science and Technology, Murthal (Sonepat), 131039, India, [b]Crystal Growth and X-ray Analysis, CSIR-National Physical Laboratory, Dr K. S. Krishnan Road, New Delhi, 110 012, India, [c]Academy of Scientific and Innovative Research, CSIR-National Physical Laboratory, New Delhi, 110012, India, [d]Materials Physics and Engineering Division, CSIR-National Physical Laboratory, Dr K. S. Krishnan Road, New Delhi, 110 012, India, and [e]TEMA-NRD, Mechanical Engineering Department, Aveiro Institute of Nanotechnology (AIN), University of Aveiro, Aveiro, 3810-193, Portugal. Correspondence e-mail: bhagavan@nplindia.org

The growth of good quality bulk single crystals of bismuth selenide by employing a high-temperature vertical Bridgman technique with a specially designed ampoule having a provision for a necking process is reported. Several growth experiments were performed and reproducible results were obtained. The crystal structure and lattice dimensions were confirmed by powder X-ray diffraction (PXRD), the bulk crystalline perfection was assessed using high-resolution X-ray diffractometry and the good bulk crystalline perfection with an indication of layered structure was confirmed. Transmission electron microscopy (TEM) was carried out for the grown single crystal and confirmed the layered structure. High-resolution TEM (HRTEM) was also used to further assess the crystalline perfection. The direct measurement of *d* spacing obtained from HRTEM imaging was found to be in good agreement with the data obtained from PXRD. The thermal behavior was examined by differential scanning calorimetry and a sharp melting was found at 983 K, which revealed the purity of the bismuth selenide. The Seebeck coefficient and electrical and thermal conductivities were measured, and a thermoelectric figure of merit was calculated in order to assess the suitability of the crystal for thermoelectric applications such as refrigeration and portable power generation. Nanoindentation analysis was also performed for the first time.

1. Introduction

Bismuth selenide is a renowned compound of the A_2B_3 chalcogenide family (A = Bi/Sb, B = Te/Se). At room temperature, bismuth telluride (Bi_2Te_3) possesses quite good thermoelectric properties, but the high cost of tellurium, due to its scarcity and toxicity, compel the use of a substitute, *i.e.* Bi_2Se_3 (Saeed *et al.*, 2014). For the past few years Bi_2Se_3 has been widely used as a three-dimensional topological insulator, which is a new class of material (Hruban *et al.*, 2011). Bismuth selenide is also a semiconductor material, having a very small direct band gap of 0.35 eV. It has a layered structure consisting of five layers of atoms in a hexagonal plane composing a rhombohedral lattice. The five layers are arranged as Se(1)–Bi–Se(2)–Bi–Se(1) and form quintuple layers (Hruban *et al.*, 2011). A weak van der Waals force field was found between the planes of Se atoms of two different quintuple layers, which permits the easy cleavage of the crystal along that plane (Choi *et al.*, 2004; Nascimento *et al.*, 1999). There is no literature available that gives an exhaustive description of the bulk single-crystal characterization of crystalline perfection or the nanoindent behavior of the title compound, which is essential knowledge for gauging the suitability of the compound for making thermoelectric devices. The device efficiency of a thermoelectric material can be assessed by the figure of merit (Janíček *et al.*, 2009).

Here, we report the growth of bismuth selenide single crystals using a vertical Bridgman high-temperature melt growth technique (VBT) and adopting the novel technique of necking, which is otherwise common in the Czochralski (CZ) technique (Bhagavannarayana, Kushwaha *et al.*, 2011). It should be mentioned that bismuth selenide is a reactive material in open atmosphere at high temperatures and hence the VBT method was chosen for crystal growth. Therein, the VBT ampoule, after the raw material had been placed into it, was evacuated up to $\sim 10^{-6}$ Torr (1 Torr = 133.3 Pa), which is not that easy in the CZ technique. Powder X-ray diffraction analysis was performed to confirm the structure and to measure the lattice dimensions. The crystalline perfection was assessed by high-resolution X-ray diffraction (HRXRD) and

high-resolution transmission electron microscopy (HRTEM) analysis. The melting point and different phase formations were identified from differential scanning calorimetry (DSC) (Setnescu *et al.*, 2010). A figure of merit for thermoelectric efficiency was determined by measuring the Seebeck coefficient and thermal and electrical conductivities using a laser flash technique. The grown crystal was also subjected to nanoindentation analysis with different loads for the first time.

2. Experimental

2.1. Crystal growth

In the present experimental study, bismuth selenide single crystals were grown successfully using VBT. Highly pure bismuth(III) selenide powder (vacuum deposition grade 99.999%) was taken as the raw material for the crystal growth process. By considering the material behavior, we made the ampoule, in comparison with the conventional conical type, in such a way that one can get a good quality single crystal. In this design, we introduced a bulb with a conical V-shaped tip at the bottom (Fig. 1*a*), from where the initial growth starts as the tip slowly moves into the colder zone. The bulb is followed by a narrow capillary with an inner diameter of ∼1 mm through which necking starts, which is generally adopted in the Czochralski crystal growth technique to prevent the dislocations from the seed crystal passing into the bulk crystal (Bhagavannarayana, Kushwaha *et al.*, 2011). The capillary also allows unidirectional growth and arrests the formation of structural grain boundaries in the bulk crystal that grow in the main ampoule as it is further lowered down into the cold zone. In the cold zone, the melt solidifies and forms into the bulk single crystal in the same direction as it was started at the bottom V-shaped tip.

The ampoule was well cleaned with soap solution followed by acetone and dried in an oven. It was then charged with the raw material of bismuth selenide, evacuated to $\sim 10^{-6}$ Torr and sealed carefully. The ampoule was hung inside a single-zone resistive furnace. The thermal profile of the resistive

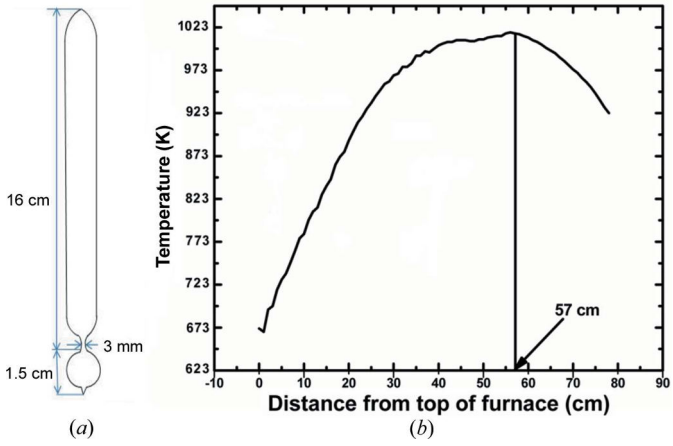

Figure 1
(*a*) Schematic diagram of ampoule and (*b*) temperature profile curve of the furnace.

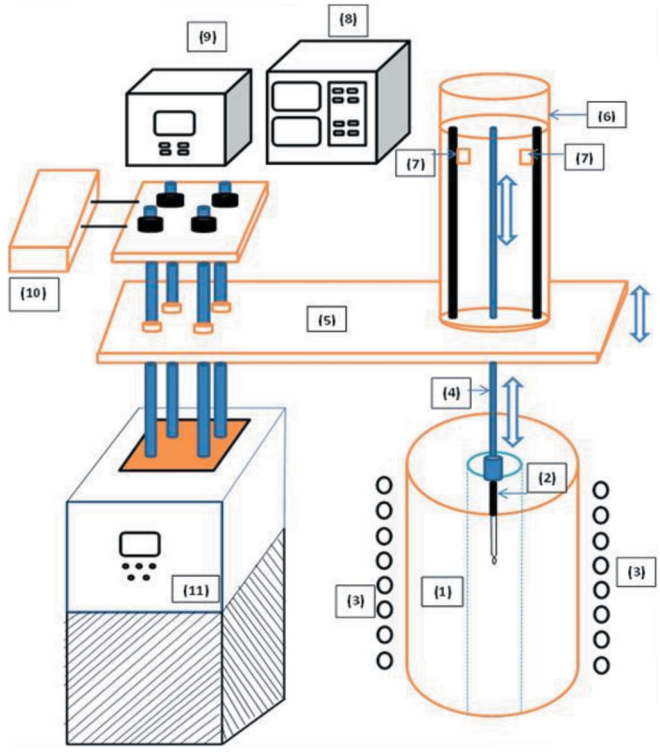

Figure 2
Schematic diagram of the vertical Bridgman setup: (1) furnace, (2) ampoule holder, (3) coils, (4) moving rod for translation of ampoule, (5) vertical movable mechanical stand, (6) cylinder containing stepper motor, (7) stepper motor, (8) nanotranslation controller, (9) furnace temperature controller, (10) motor for mechanical stand, (11) controller for mechanical stand.

furnace is shown in Fig. 1(*b*). The rate of lowering the ampoule required to produce a good quality crystal varies from material to material, depending on the material's molecular and crystalline complexity (Vijayan *et al.*, 2004). In this experiment, we have adopted 1.8 mm h^{-1} by using the nano-translation setup. A schematic representation of the setup is given in Fig. 2. The temperature of the furnace is fully controlled by a Eurotherm temperature controller having an accuracy of 1 K. The temperature is slowly increased in different steps to reach up to 993 K. This is slightly higher than the melting point (∼980 K) (Augustine & Mathai, 2001) for producing the homogenous melting of the compound. After reaching the homogenous melting point, the ampoule was kept stationary for 4 h. After that, the cooling process was started by lowering the ampoule into the cold zone, and the cooling continued

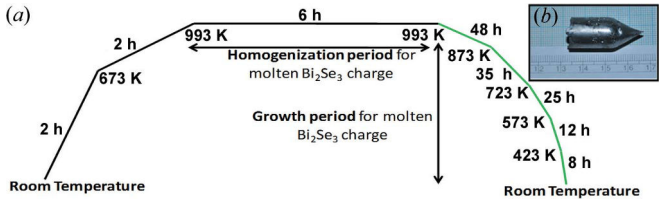

Figure 3
(*a*) Profile curve for the crystallization process and (*b*) ingot of the as-grown Bi_2Se_3 crystal.

until the crystallization process was complete. Post-growth cooling was done both by lowering the sample (into the cold zone with gradual reduction of temperature) and by subjecting the sample to different cooling rates in different temperature ranges until the temperature of the crystal reaches room temperature, as depicted in the temperature profile given in Fig. 3(*a*). After successful completion of the experiment, an ingot of length 30 mm and diameter 18 mm was obtained, which is shown in Fig. 3(*b*).

2.2. Characterization

The grown single crystals were subjected to various characterization analyses in order to check their suitability for device applications. The phase identification of the grown crystals was done on a Rigaku powder X-ray diffractometer at ambient temperature. The crystalline perfection was assessed with a PANalytical X'Pert PRO MRD high-resolution XRD system. The morphology and lattice spacing were observed using transmission electron microscopy (HRTEM, Technai G30 S-twin, 300 kV). Thermal studies were carried out by DSC. The mechanical behavior was examined by the nanoindentation technique. The thermoelectric figure of merit was estimated by measuring the Seebeck coefficient and thermal and electrical conductivity.

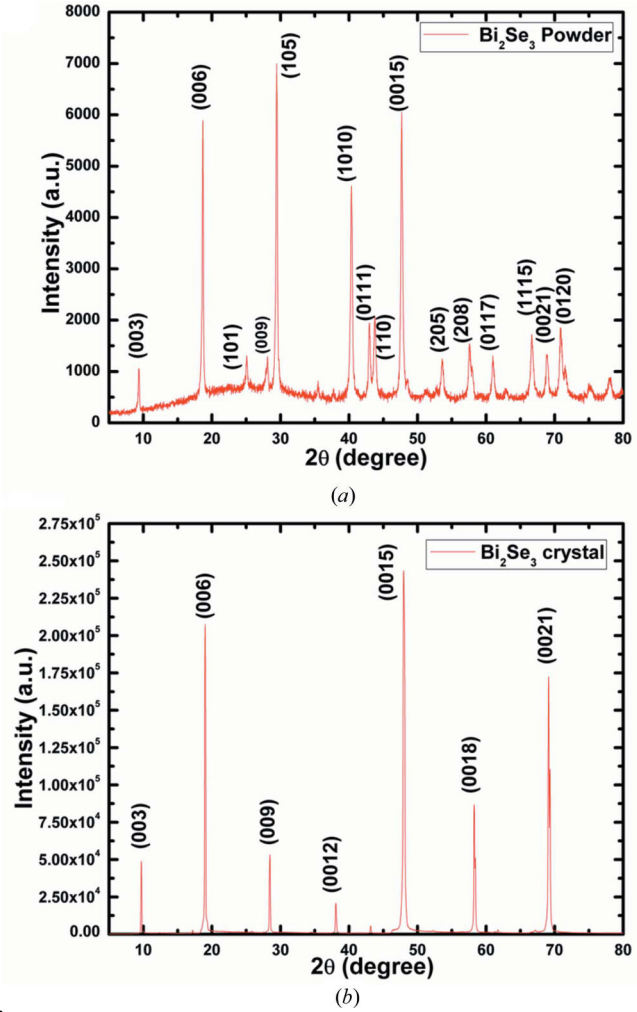

Figure 4
(*a*) Powder XRD spectrum of as-grown Bi_2Se_3 and (*b*) XRD spectrum of as-grown Bi_2Se_3 cleaved single crystal.

3. Results and discussion

3.1. X-ray diffraction analysis

The powder X-ray diffraction (PXRD) spectrum was recorded for the charge material on a Rigaku diffractometer with Cu $K\alpha$ radiation of wavelength 1.54 Å at a scan speed of 4° min^{-1} with a 2θ range of 5–80°. The recorded PXRD pattern, shown in Fig. 4(*a*), revealed that bismuth selenide crystallizes as a hexagonal structure (Augustine & Mathai, 2001). The lattice parameters for the bismuth selenide single crystal were calculated by the *Chekcell* software (http://www.ccp14.ac.uk/tutorial/lmgp/achekcelld.htm): a = 4.133, c = 28.6016 Å and V = 423.16 Å^3. These values are in close agreement with the reported JCPDS data file (No. 01-078-3528). The grown ingot was carefully cleaved and then subjected to a θ–2θ scan just as for the powder X-ray diffraction experiment, adopting the same conditions used for raw polycrystalline powder material. The recorded pattern is shown in Fig. 4(*b*), in which it is clear that the specimen is a single crystal with a cleavage plane along the [001] direction. One can see many reflections of the type 00l (l being a multiple of three as expected for a hexagonal crystal) in the PXRD spectrum of Fig. 4(*b*), in good agreement with the reported XRD spectra (Cao *et al.*, 2013; Jiao *et al.*, 2012). This further indicates the layered structure with Bi and Se atoms arranged in the form of Se(1)–Bi–Se(2)–Bi–Se(1) normal to the c axis. The crystalline perfection of the grown crystal was assessed using HRXRD and is discussed in detail in the next section.

3.2. High-resolution XRD analysis

A PANalytical X'Pert PRO MRD high-resolution XRD system with Cu $K\alpha_1$ radiation was employed to assess the crystalline perfection of the grown crystal. The rocking curves of the crystals for the diffraction planes were recorded in symmetrical Bragg geometry using the natural facets with an ω scan (Bhagavannarayana & Kushwaha, 2010) with double-axis geometry. The monochromated X-ray beam incident on the specimen was obtained using a high-resolution four-bounce Ge(220) monochromator. The diffracted beam from the specimen was detected using a scintillation detector without using any analyzer at the receiving stage (*i.e.* before the detector) to get all of the possible information such as the individual peaks from structural grain boundaries and scattered intensity from the dislocations and other defects from the specimen crystal, as described elsewhere (Bhagavannarayana & Kushwaha, 2010). Fig. 5 shows the high-resolution X-ray rocking/diffraction curve (DC) recorded for the (006) diffraction planes using Cu $K\alpha_1$ radiation for a typical Bi_2Se_3 single-crystal specimen. In the first instance, one can see that the curve contains a single, sharp and good intensity peak. However, on close observation, one can realize that the curve also contains a small but clear peak at 2330″ away from the

main peak. One can further see that there is a good scattered intensity on both sides of the main peak. On deconvolution of the diffraction curve with a Lorentzian fit, it is clear that the curve contains two additional peaks, which are 530 and 2330″ away from the main peak. The additional peak at 2330″ away from the main peak represents an internal structural low-angle grain boundary. For better understanding, a schematic of a structural grain boundary is given in the inset of Fig. 5. As seen in the inset, two regions of the crystal are misoriented by a finite angle α, also known as the tilt angle. The tilt angle may be defined as the misorientation angle between the two crystalline regions on either side of the structural grain boundary. The two regions may be perfect. If the value of α is $\leq 1'$, we may call it a very low angle boundary. If $\alpha > 1'$ but less than a degree, we call it a low-angle boundary. For more details of such structural grain boundaries including their effect on physical properties, please refer to papers by Bhagavannarayana & Kushwaha (2010) and Bhagavannarayana *et al.* (2005) and references therein. The angular separation between the two peaks gives the tilt angle α. Therefore, the tilt angle for the low-angle boundary at 2330″ from the main peak (belonging to the main crystal block) is 2330″. The FWHMs of the main peak and the low-angle boundary are 240 and 120″, respectively. The low FWHM values of the main crystal and the low-angle boundary indicate that the crystalline perfection of the specimen is quite good. However, the broad (2800″ FWHM) and very low intensity peak, which was indeed needed for the best fit, indicates that the crystal also contains mosaic blocks which are misoriented to each other by a few arc minutes. These kinds of structural defects are probably due to the layered structure of the present crystal. Even in soft organic crystals such as benzimidazole, such boundaries were found (Vijayan *et al.*, 2006). In our later investigations, such defects were found to be controlled by using a double-walled VBT ampoule to minimize the thermal fluctuations (Riscob *et al.*, 2013). However, the present VBT ampoule is designed for a fine necking process (Bhagavannarayana, Kushwaha *et al.*, 2011) and seems to be more effective at controlling the boundaries even in the very soft and layered structure. It may be mentioned here that such minute defects could be detected with well resolved peaks in the diffraction curve only because of the high resolution of the diffractometer with a four-bounce monochromator crystal. As explained in a previous article (Bhagavannarayana & Kushwaha, 2010), to detect the minute boundaries, which may even be well misoriented from the main block, and to collect the scattered intensity from the loosely bound layers, a simple ω scan was used instead of the ω–2θ scan. Since the main crystal block has reasonably good crystalline perfection, such defects may not have much influence on the physical properties, as shall be discussed in the following section. However, a quantitative analysis of such defects, which are often unavoidable owing to the nature of the material and the growth method, is of great importance in certain device applications, for example, phase matching applications in nonlinear optical crystals (Bhagavannarayana, Riscob & Shakir, 2011) and piezoelectric applications (Bhagavannarayana, Budakoti *et al.*, 2005).

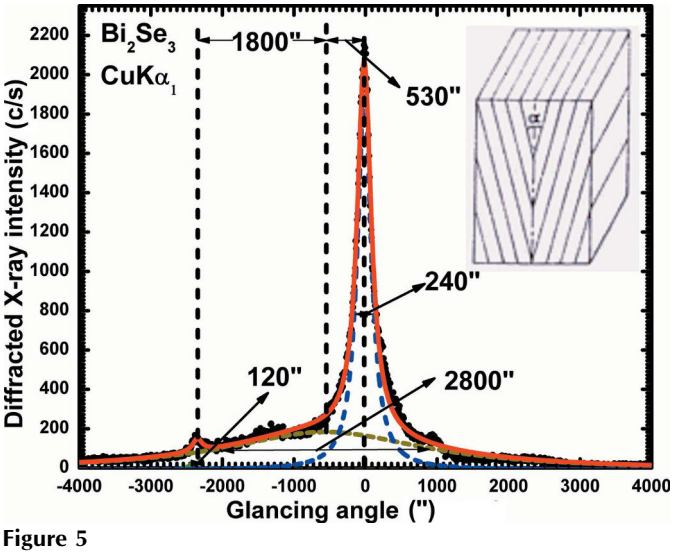

Figure 5
High-resolution diffraction curve recorded for (006) planes in symmetrical geometry for the cleaved crystal.

3.3. Transmission electron microscopy

Morphological studies and further assessments of crystalline perfection studies were carried out by TEM and high-resolution TEM (Technai G30 S-twin, 300 kV), respectively. The TEM image that is given in Fig. 6(*a*) reveals that the grown single crystal has different sheets of atoms. This is in complete agreement with the reported crystal structure of bismuth selenide (Irfan *et al.*, 2014), which has different hexagonal layers of atoms within the rhombohedral unit cell. An HRTEM image of the present crystal is shown in Fig. 6(*b*). One can clearly see the well defined parallel fringes of atomic planes. This indicates that the sample has very high crystalline perfection, which is in agreement with the HRXRD results. The measured interplanar *d* spacing between lattice fringes from the HRTEM image is equal to 0.210 nm, which is well matched with that of the JCPDS file No. 01-078-3528, corresponding to the *hkl* planes of (0111).

3.4. Differential scanning calorimetry

Differential scanning calorimetry is used to characterize the thermal phenomena such as phase transitions, melting/crystallization behavior, degree of crystallinity, oxidative stability, purity, thermo kinetics of various processes *etc.* (Setnescu *et al.*, 2010). DSC analysis was carried out by using a Mettler Toledo instrument in an argon atmosphere (Model No. HT LF1). A sample of 5–10 mg was placed in an alumina crucible and the experiment was performed in the temperature range of 303–1000 K. In the DSC spectrum, which is shown in Fig. 7, one can see an endothermic peak at around 981 K, which is close to the melting temperature of bismuth selenide (Augustine & Mathai, 2001). It also implies that no other phase formation occurs during the growth process. The sharpness of the endothermic peak observed by DSC shows the good degree of crystallinity in the sample, which is in accord with the observed HRXRD analysis. This measurment

reveals that the title compound can withstand high temperature, which is mandatory for device fabrication related to thermoelectric applications.

3.5. Thermoelectric properties

The efficiency of a thermoelectric material is governed by its figure of merit (ZT), which is a dimensionless quantity. It is defined as a quantity consisting of the Seebeck coefficient (S given in the units V K^{-1}), electrical conductivity (σ given in Ω^{-1} m^{-1}) and thermal conductivity (κ in W m^{-1} K^{-1}). Mathematically, ZT is defined by the formula

$$ZT = S^2\sigma T/\kappa, \quad (1)$$

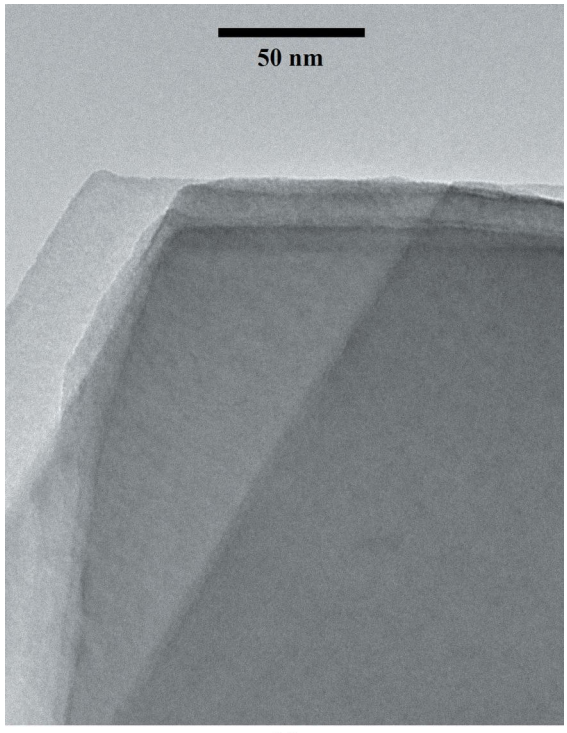

(*a*)

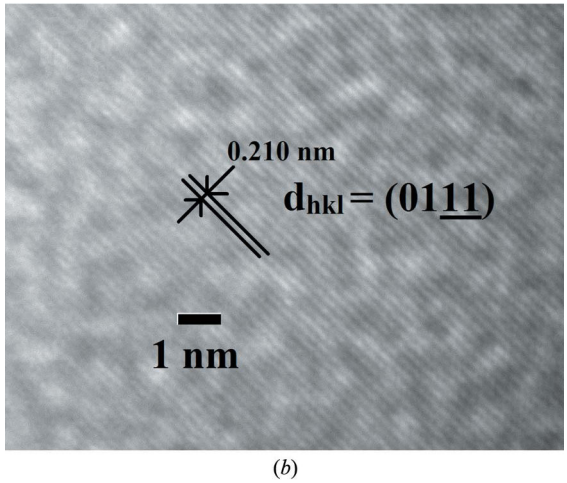

(*b*)

Figure 6
(*a*) TEM image of a Bi_2Se_3 single crystal showing the layered structure and (*b*) HRTEM image showing lattice fringes.

where T is the temperature in K (Janicek *et al.*, 2009). In the present study, the thermoelectric properties of the title crystal were measured in the temperature range of 303–423 K. A rectangular shaped specimen (1 × 4 × 12 mm) was used for the Seebeck coefficient and electrical conductivity measurements. These measurements were carried out using a ZEM-3 apparatus (ULVAC-RIKO, Japan) in a helium inert gas atmosphere (Muthiah *et al.*, 2013). The thermal diffusivity measurement was carried out on a circular disc sample having a diameter of 12.7 mm, using an LFA-1000 (Linseis, Germany) instrument under vacuum (Muthiah *et al.*, 2014). The thermal conductivity of the material was calculated using the formula $\kappa = D\,c_p\,\rho$, where D is the density, c_p is the specific heat value and ρ is thermal diffusivity. The specific heat was measured by DSC.

3.5.1. Seebeck coefficient. In Fig. 8, it can be seen that the Seebeck coefficient has a negative value in the entire temperature range, which implies that our single crystal shows

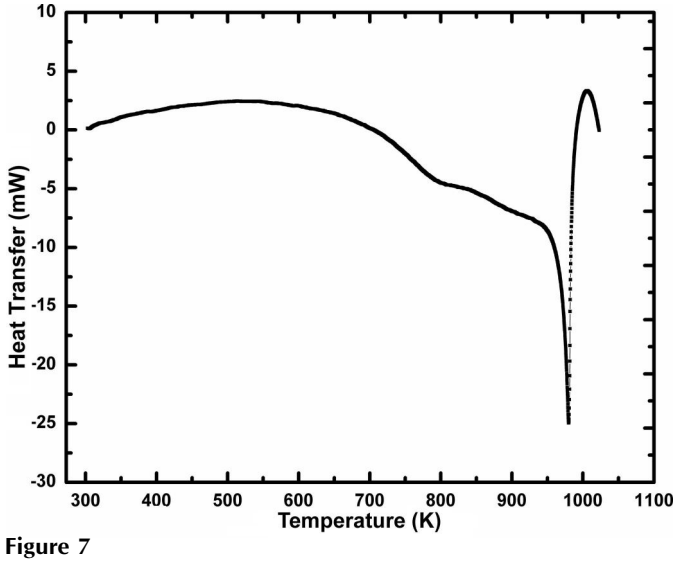

Figure 7
DSC spectrum for Bi_2Se_3.

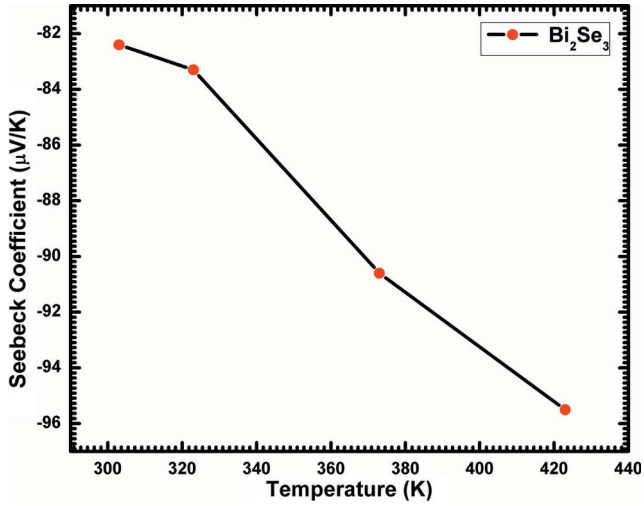

Figure 8
Temperature dependence of the Seebeck coefficient.

n-type conductivity. This is supported by previous studies (Saeed *et al.*, 2014; Janíček *et al.*, 2009) and is due to the vacancies of the Se atoms. In comparison with the reported data (Janíček *et al.*, 2009) for a Bi_2Se_3 crystal grown by the same method of VBT with a conventional cone-shaped ampoule, the value of the Seebeck coefficient found in the present investigation is quite high. This can be attributed mainly to the good crystalline quality of the grown crystal, as found in the HRXRD analysis, which was made possible by adopting necking, as demonstrated in our recent investigation on LiF crystals (Bhagavannarayana, Kushwaha *et al.*, 2011). In the present investigation, the initial crystal was started in the bulb portion and the fine crystal growth was elongated through the 1 mm-diameter narrow portion of the VBT ampoule. This type of arrangement seems to be useful and is essential in layered structures or soft organic materials.

3.5.2. Electrical and thermal conductivities. In Fig. 9, one can see the temperature dependence of the electrical conductivity as well as thermal conductivity. Electrical conductivity decreases and thermal conductivity increases with an increase in temperature. The thermal conductivity is given by $\kappa = \kappa_e + \kappa_l$, where κ_e and κ_l represent the electronic and lattice parts of the thermal conductivity, respectively. In metals the κ_e value dominates, while in semiconductors the κ_l value dominates, which is also related to the phonon scattering. The phonon scattering is more effective in irregular or disordered materials and decreases the thermal conductivity. In the present crystal, the high crystalline perfection might have led to the increase in the thermal conductivity.

3.5.3. Figure of merit. The figure of merit ZT was calculated from equation (1) and is plotted against temperature as shown in Fig. 10. At low temperatures ZT increases sharply, but at higher temperatures it increases slowly as the thermal conductivity dominates at higher temperatures. The highest value of ZT for the grown single crystal is ~0.75 at 423 K. Very few references are available in the literature to compare the measured ZT value of Bi_2Se_3 in the bulk single-crystal form. Kulbachinskii *et al.* (2012) studied Bi_2Se_3 in its single-crystal form. The ZT value was measured in the temperature range from 7 to 300 K with a measured value of ~0.1 at 300 K. Our lowest temperature at which ZT was measured is 303 K, with an experimentally obtained value of ~0.6. In Zuo's dissertation (Zuo, 2011), the ZT value for pure and single crystals with excess Se (Bi_2Se_{3+x}) was reported. The highest ZT value of 0.58 and lowest ZT value of 0.29 were obtained for the samples with $x = 0$ at 425 K and $x = 0.24$ at 320 K, respectively. These results indicate that, with excess Se, the ZT value was decreased and hence the pure compound of Bi_2Se_3 seems to be good. Though the temperature range is different, we can compare our ZT value with that of Zuo's highest value of 0.58 measured at 425 K as our measured temperature (423 K) is very close to Zuo's value, *i.e.* 425 K. Our ZT value (0.75) is much higher than the reported value of 0.58. Similarly, one can find another article (Kadel *et al.*, 2011) on the title compound, but it was studied in the nanocrystalline form. The reported ZT value at 423 K is around 0.06. Another report by Soni *et al.* (2012) on nanostructured $Bi_2Te_{3-x}Se_x$ alloy was also found with different x values, wherein the ZT value for Bi_2Se_3 ($x = 3$) is −0.1 at 323 K. Our measured value for ZT at this temperature is ~0.7. The obtained result was compared with the reported results and the value of ZT for the grown crystal seems to be reasonably high. From HRXRD and HRTEM studies one can attribute this high ZT value to the good crystalline perfection. It may be mentioned here that, in a layered structure crystal, the electrical conductivity along the two-dimensional layered surface decreases owing to defects, whereas the thermal conductivity increases in the direction perpendicular to the layered surface. These two consequences lead to a decrease in the value of the figure of merit. This study confirms these facts and reveals that crystalline perfection has a crucial role in getting a good figure of merit for thermoelectric applications.

3.6. Nanoindentation analysis

Nanoindentation analysis was performed to obtain two mechanical quantities, *i.e.* the modulus of elasticity and hardness. As the name suggests, in this analysis we need a load

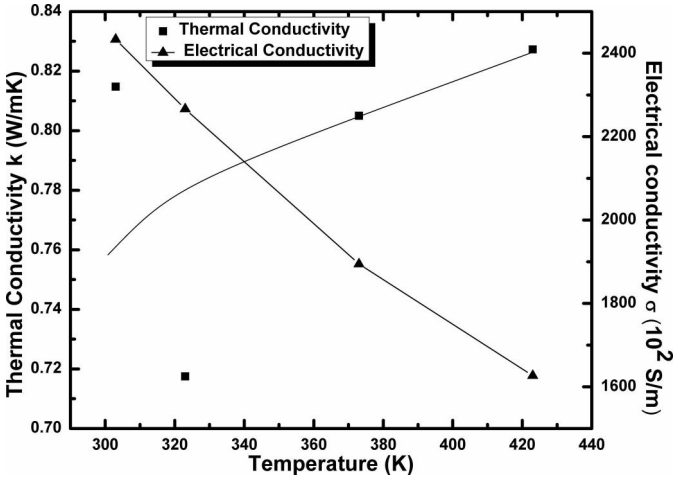

Figure 9
Temperature dependence of the electrical and the thermal conductivities.

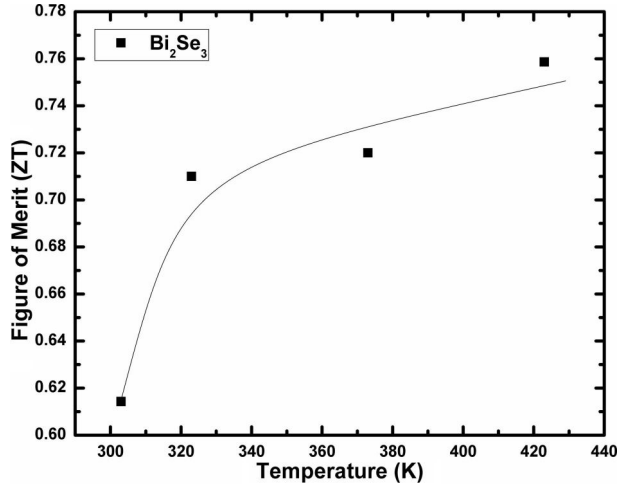

Figure 10
Figure of merit *versus* temperature.

having a value in millinewtons and a penetration depth of the indenter in nanometres; thus the area required for the analysis is very small. It is helpful to correlate the mechanical properties of the sample with its atomic arrangement in a particular plane of atoms. From the device application point of view, the mechanical property analysis has great importance. In the nanoindentation test, the depth of indent is measured as the load is applied to the indenter. The known geometry of the indenter allows the size of the area of contact to be determined. Thus we obtained a plot between peak load and displacement of the indenter inside the sample. The plot is known as the load–displacement curve. The indenter used in this analysis was a three-sided pyramidal Berkovich diamond indenter having nominal edge radius of 20 nm (faces 65.3° from vertical axis). The indentation was applied on the cleaved surface normal to the planar surface of (001) of the sample by the nanoindenter (TTX-NHT, CSM instruments), which is fully calibrated (Bdikin *et al.*, 2014). The load range used was from 5 to 150 mN, having an approach speed of 2000 nm min^{-1}. We maintained a constant loading and unloading speed of 20 mN min^{-1} throughout the measurement, having a dwell time of 10 s between the loading and the unloading step. Using the Oliver and Pharr standard method (Jat *et al.*, 2013), nine indentations were made on the cleaved surface of the bismuth selenide crystal.

The hardness can be calculated by the formula

$$H = F_{\max}/A_c, \tag{2}$$

where $F_{\max}$ is the maximum indentation load and A_c is the contact area of the indentation. The area is calculated from the calibrated indenter tip and is a function of the contact depth (h_c). Next a calculation of the slope ($S_h = dP/dh$) of the unloading curve in the load–displacement plot was made by measurement of the contact depth using the formula

$$h_c = h_{\max} - \varepsilon\left(F_{\max}/S_h\right), \tag{3}$$

where $h_{\max}$ is the total displacement for maximum indentation load and ε is the indenter constant (0.75) for the Berkovich indenter tip. The unloading portion of the load–displacement curve is related as

$$F = \alpha(h - h_f)^m, \tag{4}$$

where F is the indentation load, h is the displacement of the indenter, h_f is the final displacement of the indenter after unloading is complete, while α and m are empirical parameters. The values of these parameters were obtained by using a curve fitting technique. Then we calculate the value of S_h by differentiating equation (3) at maximum depth of penetration, $h_{\max}$:

$$(dP/dh)_{h=h_{\max}} = S_h = \alpha m(h_{\max} - h_f)^{m-1}. \tag{5}$$

In the load–displacement curve given in Fig. 11, we observe a pop-in which is due to plastic deformation during loading, while unloading elastic deformation is observed. The presence of pop-ins is due to the plastic nature of the crystal. Hence, we can say pop-ins imply an elastic to plastic transition, also known as a displacement burst, on the load–displacement (F–d) curve (Varughese *et al.*, 2013). An F–d curve with pop-ins also implies a weak bond, *i.e.* the van der Waals interaction, between Se atoms of two different planes, along which the crystal can be easily cleaved (Varughese *et al.*, 2011). These pop-ins are also attributed to homogeneous or heterogeneous nucleation of dislocations under the indenter tip (Varughese *et al.*, 2013). In the case of bismuth selenide single crystals, these pop-ins tend to be heterogeneous. The breaking of the molecular stack results in a sudden penetration of the indenter deeper into the sample, which is reflected by a pop-in. Fig. 12 shows the profile of a cross section image of the depth after a load of 50 mN was applied on the sample by the indenter. In the insets in both Figs. 11 and 12, an imprint of the indent is shown, in which one can see the pile-ups. A good agreement was seen between Figs. 11 and 12. Table 1 contains the various

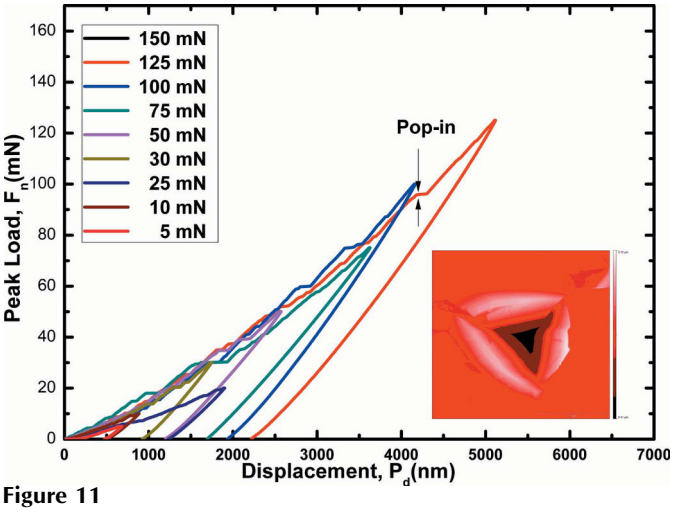

Figure 11
Load *versus* displacement curve for a bismuth selenide single crystal. The inset in the figure shows a typical imprint made after indentation on the (001) planar surface.

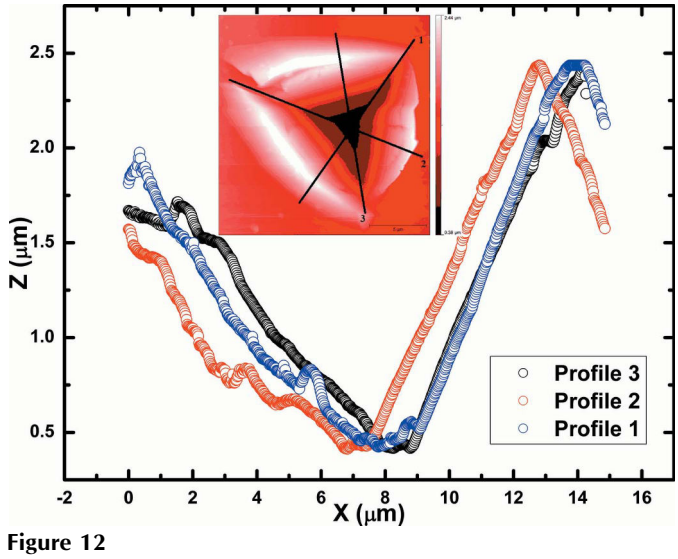

Figure 12
Profile for the indentation mark on the sample. The inset shows the topographic image of the indentation imprint made by the indenter.

Table 1
Various parameters measured in nanoindentation analysis.

F (mN)	H_{IT} (MPa)	E_{IT} (GPa)	H_v	h_m (nm)	S (mN nm^{-1})	h_c (nm)	h_r (nm)	h_p (nm)	m
5	661.902	9.073	61.299	681.6	0.032	557.787	522.932	475.039	1.26
10	976.14	8.203	90.401	884.241	0.033	647.628	583.991	505.71	1.224
30	839.579	5.85	77.754	1746.779	0.045	1207.026	1073.394	930.1	1.176
50	762.855	4.178	70.649	2573.423	0.043	1634.593	1415.197	1205.146	1.151
75	615.84	3.132	57.033	3628.238	0.044	2227.615	1930.01	1697.026	1.112
100	565.06	3.185	52.331	4165.172	0.054	2684.909	2318.522	1950.316	1.176
125	487.858	2.573	45.181	5117.825	0.053	3230.658	2744.18	2237.433	1.194
150	437.298	2.168	40.491	6059.92	0.051	3737.795	3138.954	2551.82	1.194

F: peak load; H_{IT}: indentation hardness; E_{IT}: indentation modulus; H_v: Vickers hardness; h_m: maximum indentation depth; S: stiffness; h_c: contact depth of indenter; h_r: tangent depth, *i.e.* point of the tangent to the unloading curve at maximum load with the indentation depth axis; h_p: permanent indentation depth after removal of force; m: empirical parameter.

results that were obtained by the analysis of load–displacement curves along the [001] direction.

3.6.1. Hardness analysis. The hardness analysis was performed on the cleaved surface of the bismuth selenide single crystal normal to the (001) plane. A plot between the peak load and the contact depth can be seen in Fig. 13(*a*). One can easily observe the increment in the contact depth with the increment in the peak load. This happened owing to the significant decrease in the hardness value of the crystal. The calculated values of the hardness of the bismuth selenide single crystal in the (001) plane are obtained from the best fit value of the contact depth as a function of peak load. In Fig. 13(*a*) one can also observe that, as the load increases, the value of contact depth also increases. This clearly happened owing to significant decrement in the hardness of the title compound with increase in the load. The increasing value of the contact depth h_c can also be correlated with the indentation size d. Thus we have a relation between peak load and contact depth as (Jat *et al.*, 2013)

$$F = a_0 + a_c h_c + a_2 h_c^2. \quad (6)$$

In Fig. 13(*a*), the curve is fitted with the polynomial function and the fitted values for a_2 are found to be 2.084×10^{-6} mN nm^{-2}. The parameter a_2 and independent hardness H_0 are related by

$$H_0 = k a_2, \quad (7)$$

where k is equal to 1/24.5 for the Berkovich indenter. Thus, the calculated value of independent hardness H_0 for the (001) plane is 85.09 MPa.

3.6.2. Elastic modulus. From the load–displacement curves, one can obtain the value of Young's modulus by extracting the data. Young's modulus *versus* the log value of the peak load is shown in Fig. 13(*b*). One can observe a decrease in the value of Young's modulus with the increase in the value of peak load. In Fig. 13(*c*), the dependence of the stiffness on the contact depth can be observed. The relation of S with h_c is given as (Jat *et al.*, 2013)

$$S = a + b h_c. \quad (8)$$

The above equation represents the linear relationship between the stiffness and contact depth. The value of the slope, *i.e.* b, of the plot between S and h_c gives the value of the

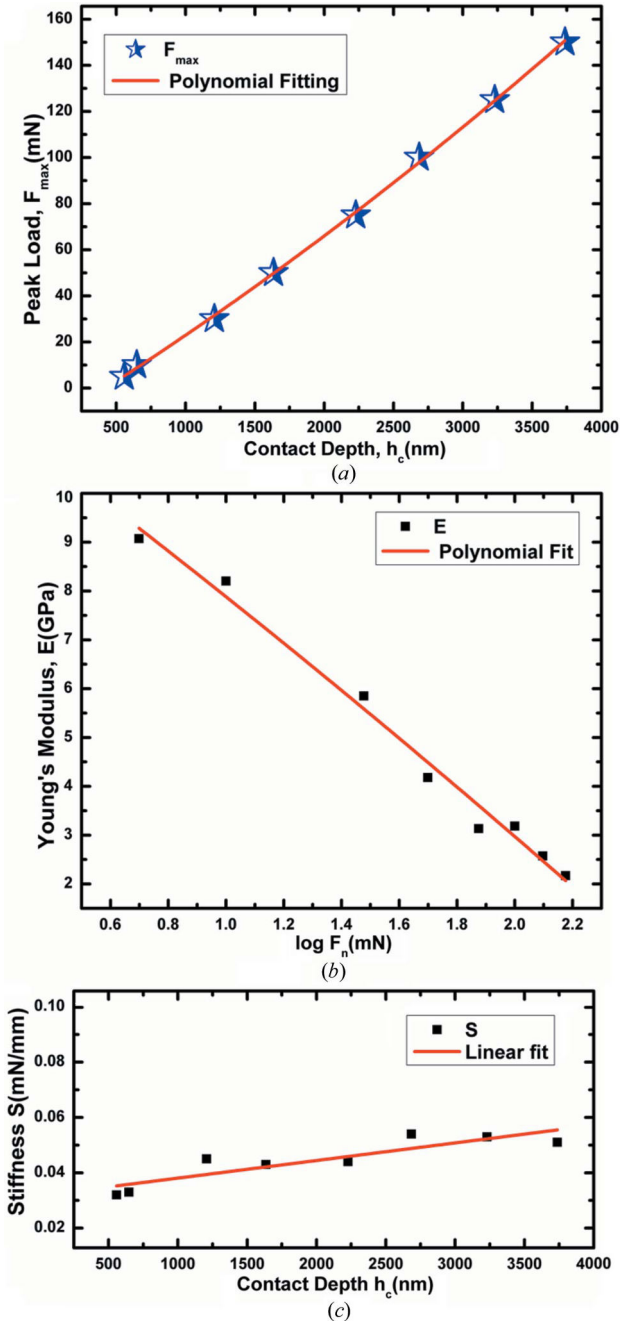

Figure 13
(*a*) Contact depth dependence of peak load, (*b*) Young's modulus *versus* peak load and (*c*) stiffness *versus* contact depth.

elastic modulus E, and thus the calculated value of E is 6.361 GPa. The small value of hardness as well as the elastic modulus agreed with the soft plastic nature of the Bi_2Se_3 single crystal at the cleavage plane.

3.7. Conclusion

The novel approach of necking was introduced with a specially designed ampoule in the VBT method, and good quality pure Bi_2Se_3 bulk single crystals were thus grown successfully. The lattice dimension and crystalline perfection were assessed by PXRD, HRXRD and HRTEM analyses. The thermal stability and the phase transition were examined by the DSC technique and it was observed that no other phase was formed during the growth process. The figure of merit (ZT) was evaluated at different temperatures in the range from 303 to 423 K. We found that the highest value of ZT is 0.75 at 423 K. This value and the value at 303 K are compared with the available literature, and to the best of our knowledge, the ZT values observed in the entire measured temperature range from 303 to 423 K are found to be higher than those reported in the literature, either for bulk crystals or for nanocrystalline structures. This result is attributed to the good bulk crystalline perfection as observed from HRXRD. However, there is still some scope for further improvement in the crystalline perfection, the trials of which are still on going. The mechanical behavior of the title compound was assessed by the nanoindentation method for the first time, and the hardness and the elastic modulus values were calculated as 85.09 MPa and 6.361 GPa, respectively.

The authors are thankful to Professor R. C. Budhani, Director, CSIR-National Physical Laboratory, for his guidance and kind encouragement in pursuing this investigation. The authors would also like to thank Dr Vidyanand Singh, CSIR-NPL, for his valuable support in TEM analysis.

References

Augustine, S. & Mathai, E. (2001). *Mater. Res. Bull.* **36**, 2251–2261.
Bdikin, I., Singh, B., Kumar, J. S., Graça, M. P. F., Balbashov, A. M., Grácio, J. & Kholkin, A. L. (2014). *Scr. Mater.* **74**, 76–79.
Bhagavannarayana, G., Ananthamurthy, R. V., Budakoti, G. C., Kumar, B. & Bartwal, K. S. (2005). *J. Appl. Cryst.* **38**, 768–771.
Bhagavannarayana, G., Budakoti, G. C., Maurya, K. K. & Kumar, B. (2005). *J. Cryst. Growth*, **282**, 394–401.
Bhagavannarayana, G. & Kushwaha, S. K. (2010). *J. Appl. Cryst.* **43**, 154–162.
Bhagavannarayana, G., Kushwaha, S. K., Shakir, Mohd. & Maurya, K. K. (2011). *J. Appl. Cryst.* **44**, 122–128.
Bhagavannarayana, G., Riscob, B. & Shakir, M. (2011). *Mater. Chem. Phys.* **126**, 20–23.
Cao, H., Xu, S., Miotkowski, I., Tian, J., Pandey, D., Hasan, M. Z. & Chen, Y. P. (2013). *Phys. Status Solidi Rapid Res. Lett.* **7**, 133–135.
Choi, J., Lee, H. W., Kim, B. S., Choi, S., Choi, J. & Cho, S. (2004). *J. Mag.* **9**, 125–127.
Hruban, A., Materna, A., Dalecki, W., Strzelecka, G., Piersa, M., Wegner, E. J., Diduszko, R., Romaniec, M. & Orłowski, W. (2011). *Acta Phys. Pol. A*, **120**, 950–953.
Irfan, B., Sahoo, S., Gaur, A. P. S., Ahmadi, M., Guinel, M. J. F., Katiyar, R. S. & Chatterjee, R. (2014). *arXiV*: 1401:4346VI.
Janíček, P., Drašar, C., Beneš, L. & Lošťák, P. (2009). *Cryst. Res. Technol.* **44**, 505–510.
Jat, S. K., Vijayan, N., Krishna, A., Philip, J., Verma, S., Bdikin, I., Singh, B., Bhagavannarayana, G. & Halder, S. K. (2013). *CrystEngComm*, **15**, 10034–10042.
Jiao, W. H., Jiang, S., Feng, C. M., Xu, Z. A., Cao, G. H., Xu, M., Feng, D. L., Yamada, A., Matsubayashi, K. & Uwatoko, Y. (2012). *AIP Adv*. **2**, 022148.
Kadel, K., Kumari, L., Li, W. Z., Huang, J. Y. & Provencio, P. P. (2011). *Nanoscale Res. Lett.* **6**, 57.
Kulbachinskii, V. A., Kytin, V. G., Kudryashov, A. A. & Tarasov, P. M. (2012). *J. Solid State Chem.* **193**, 47–52.
Muthiah, S., Pulikkotil, J., Srivastava, A. K., Kumar, A., Pathak, B. D., Dhar, A. & Budhani, R. C. (2013). *Appl. Phys. Lett.* **103**, 053901.
Muthiah, S., Sivaiah, B., Gahtori, B., Tyagi, K., Srivastava, A. K., Pathak, B. D., Dhar, A. & Budhani, R. C. (2014). *J. Electron. Mater.* **43**, 2035–2039.
Nascimento, V. B., de Carvalho, V. E., Paniago, R., Soares, E. A., Ladeira, L. O. & Pfannes, H. D. (1999). *J. Electron Spectrosc. Relat. Phenom.* **104**, 99–107.
Riscob, B., Vijayan, N., Shakir, M., Wahab, M. A. & Bhagavannarayana, G. (2013). *J. Appl. Cryst.* **46**, 276–278.
Saeed, Y., Singh, N. & Schwingenschlögl, U. (2014). *Appl. Phys. Lett.* **104**, 033105.
Setnescu, R., Bancuta, I., Setnescu, T., Cimpoca, V., Silviu, J. & Popescu, I. V. (2010). *J. Sci. Arts*, **1**, 95–102.
Soni, A., Yanyuan, Z., Ligen, Y., Aik, M. K. K., Dresselhaus, M. S. & Xiong, Q. (2012). *Nano Lett.* **12**, 1203–1209.
Varughese, S., Kiran, M. S. R. N., Ramamurty, U. & Desiraju, G. R. (2013). *Angew. Chem. Int. Ed.* **52**, 2701–2712.
Varughese, S., Kiran, M. S. R. N., Solanko, K. A., Bond, A. D., Ramamurty, U. & Desiraju, G. R. (2011). *Chem. Sci.* **2**, 2236–2242.
Vijayan, N., Balamurugan, N., Ramesh Babu, R., Gopalakrishnan, R., Ramasamy, P. & Harrison, W. T. A. (2004). *J. Cryst. Growth*, **262**, 218–222.
Vijayan, N., Bhagavannarayana, G., Ramesh Babu, R., Gopalakrishnan, R., Maurya, K. K. & Ramasamy, P. (2006). *Cryst. Growth Des.* **41**, 784–789.
Zuo, P. Z. (2011). MSc thesis, Wuhan University of Technology, China.